International Journal of Pharmaceutics 660 (2024) 124377

Contents lists available at ScienceDirect

International Journal of Pharmaceutics

journal homepage: www.elsevier.com/locate/ijpharm

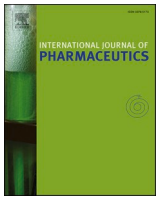

Improvement of lidocaine skin permeation by using passive and active enhancer methods

Feria Hasanpour [a], Mária Budai-Szűcs [a], Anita Kovács [a], Rita Ambrus [a], Orsolya Jójárt-Laczkovich [a], Martin Cseh [a,b], Zsolt Geretovszky [b], Ferhan Ayaydin [c,d], Szilvia Berkó [a,*]

[a] Institute of Pharmaceutical Technology and Regulatory Affairs, University of Szeged, Faculty of Pharmacy, 6 Eötvös Str., Szeged H-6720, Hungary
[b] Center of Excellence for Interdisciplinary Research, Development and Innovation, 3D Center, University of Szeged, 107 Tisza Lajos Blvd., Szeged H-6720, Hungary
[c] Functional Cell Biology and Immunology Advanced Core Facility (FCBI), Hungarian Centre of Excellence for Molecular Medicine (HCEMM), University of Szeged, 6 Korányi Ave., Szeged H-6720, Hungary
[d] Agribiotechnology and Precision Breeding for Food Security National Laboratory, Institute of Plant Biology, HUN-REN Biological Research Centre, 62 Temesvári Blvd., Szeged, H-6726, Hungary

ARTICLE INFO

Keywords:
Lidocaine
nanostructured lipid carriers (NLCs)
Dermal drug delivery
3D printed microneedles
Human skin

ABSTRACT

Lidocaine is generally recognized and preferred for local anaesthesia, but in addition, studies have described additional benefits of lidocaine in cancer therapy, inflammation reduction, and wound healing. These properties contribute to its increasing importance in dermatological applications, and not only in pain relief but also in other potential therapeutic outcomes. Therefore, the purpose of our study was to enhance lidocaine delivery through the skin. A stable nanostructured lipid carrier (NLC), as a passive permeation enhancer, was developed using a 2^3 full factorial design. The nanosystems were characterized by crystallinity behaviour, particle size, zeta potential, encapsulation efficiency measurements, and one of them was selected for further investigation. Then, NLC gel was formulated for dermal application and compared to a traditional dermal ointment in terms of physicochemical (rheological behaviour) and biopharmaceutical (qualitative Franz diffusion and quantitative Raman investigations) properties. The study also examined the use of 3D printed solid microneedles as active permeation enhancers for these systems, offering a minimally invasive approach to enhance transdermal drug delivery. By actively facilitating drug permeation through the skin, microneedles can complement the passive transport achieved by NLCs, thereby providing an innovative and synergistic approach to improving lidocaine delivery.

1. Introduction

Lidocaine is commonly recognized and preferred in local anaesthesia for its unique characteristics and wide-ranging applications in skin procedures (Bahar and Yoon, 2021). The properties of local anaesthetics depend on factors such as aromatic ring structure, linkage chain, and the alkyl group attached to amine nitrogen (Ramadon et al., 2023). They can be classified into esters and amides based on their intermediate chain. Esters, such as procaine and tetracaine, are metabolized by the liver to produce *para*-aminobenzoic acid (PABA) and may trigger allergies and contact dermatitis in dermal application, while amides, such as lidocaine, undergo metabolism primarily by plasma cholinesterase, which offers better stability and lower allergy risk compared to esters (Gordh et al., 2010) (Fig. 1).

Beyond its well-established role as a local anaesthetic, lidocaine has also shown additional benefits, including anti-cancer (Lirk et al., 2014) and anti-inflammatory effects by suppressing tumour necrosis factor alpha (TNFα) and via a mechanism related to its anti-inflammatory effects through the toll-like receptor (TLR) (Zhou et al., 2020, Garutti et al., 2014). Some studies suggest that lidocaine may have positive effects on wound healing by reducing pain intensity in various conditions, including postsurgical persistent pain (Xu et al., 2019. Ali et al., 2022), and in specific conditions such as postherpetic neuralgia, diabetic peripheral neuropathy, and chronic pain, e.g. osteoarthritis pain. These

* Corresponding author.
E-mail address: berko.szilvia@szte.hu (S. Berkó).

https://doi.org/10.1016/j.ijpharm.2024.124377
Received 4 April 2024; Received in revised form 17 June 2024; Accepted 21 June 2024
Available online 22 June 2024

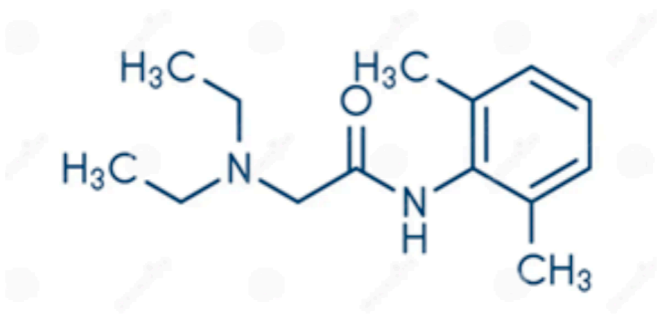

Fig. 1. Chemical structure of lidocaine.

properties contribute to its growing significance in dermatological applications and its benefits not only in pain management but also regarding potential therapeutic outcomes (Janowska et al., 2022, Treadwell et al., 2019).

The dermal drug delivery of lidocaine can be achieved by both passive and active transport methods to enhance its penetration and therapeutic outcomes. Passive methods involve optimizing the drug formulation or carrier to increase skin permeability, while active methods utilize physical or mechanical means to enhance drug transport, allowing a broader range of drugs to be effectively delivered into the skin (Brown et al., 2006; Yu et al., 2021).

The passive transport of lidocaine through the skin can be enhanced using nanostructured lipid carriers (NLCs). NLCs are a promising drug delivery system that utilizes lipid nanoparticles to improve the penetration of drugs through the skin (Yu et al., 2021, Pathak and Nagarsenker, 2009). NLCs can lead to increased drug accumulation in the epidermis and dermis, as well as in the acceptor medium, thereby enhancing the overall efficacy of transdermal drug delivery (Khan et al., 2023). This method is particularly effective for drugs with low molecular mass and sufficient hydrophobicity, which are effective in low-dose administration. Therefore, NLCs represent a valuable approach to enhancing the permeation of drug molecules across the skin, offering fast onset and prolonged drug release in deep local anaesthesia with reduced systemic absorption and side effects (Khurana et al., 2013). These findings highlight the potential of NLCs in enhancing the permeation of lidocaine across the skin, offering a valuable approach to facilitating the passive transport of lidocaine through the epidermis (Zhao et al., 2018).

As for enhancing active permeation through the skin, microneedles (MNs) can be used as a painless and minimally invasive device, known as the poke and patch approach in the skin, which facilitates dermal delivery. MNs can be characterized by different shapes (cone and pyramid) and forms (solid, drug-coated, hollow, dissolvable, and hydrogel-based microneedles). Solid microneedles are the simplest form of microneedles, where microneedles penetrate the tough barrier of the stratum corneum, creating channels for active molecular diffusion (Parhi, 2023, Dabbagh et al., 2021). The advantages of using 3D printing technology for printing microneedles include the ability to create complex structures with high precision. 3D printing, known as additive manufacturing, offers an innovative technology that constructs objects layer by layer based on a computer-aided design (CAD) model (https://www.iso.org/obp/ui/#iso:std:iso-astm:52900, xxxx). Among 3D printing technologies, Vat Photopolymerization stands out for its ability to create structures with high speed, resolution, and precision (Milliken et al., 2024). Within this category, stereolithography (SLA), which uses light irradiation to solidify liquid resin into solid objects, has found potential applications in the fields of developing and fabricating microneedle arrays with exceptional resolution and precision (Zhang et al., 2021, Lakkala et al., 2023). Additional benefits of 3D printing technology include ease of customization, making it easy to quickly modify designs to meet individual requirements (Economidou et al.,

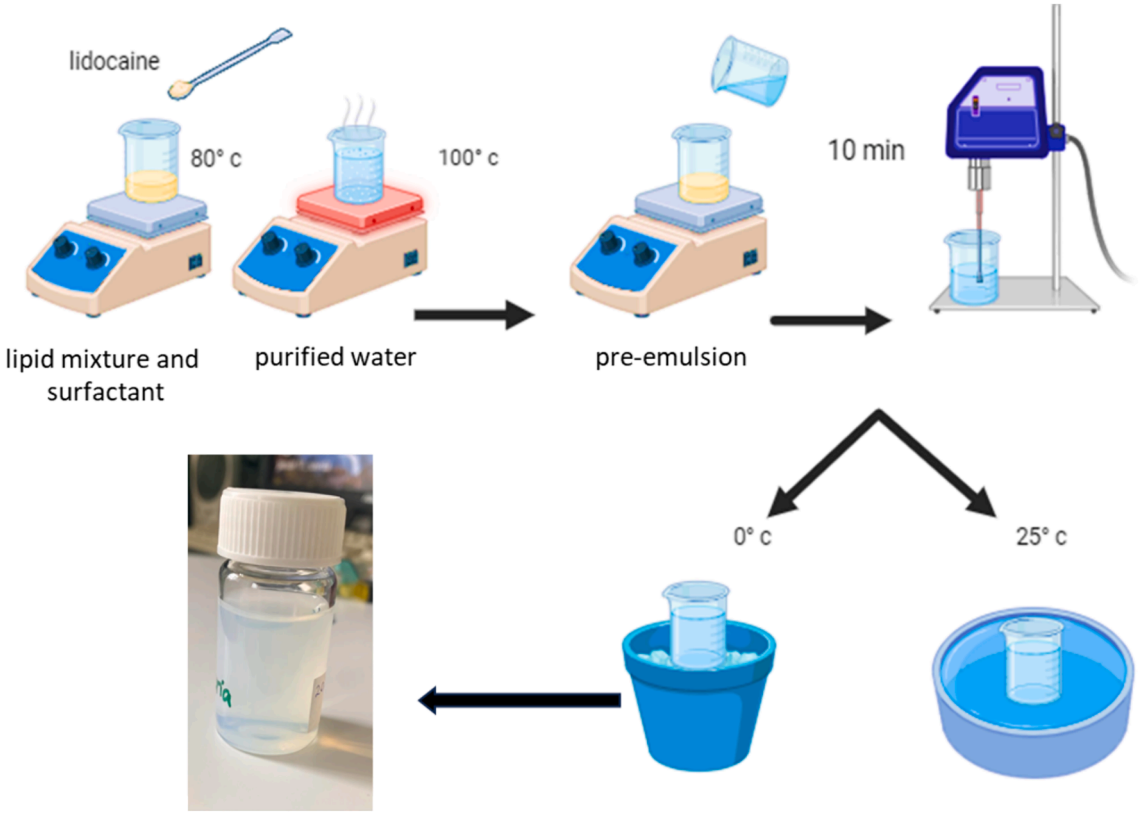

Fig. 2. Illustration of the preparation process of NLCs containing lidocaine. Part of the NLC preparation image was created with Biorender.com.

2019). This allows the adaptation of microneedles to different drug formulations, patient needs, or targeted delivery sites (Dabbagh et al., 2021; Le et al., 2023). 3D printing technology has several drawbacks, such as material limitations, biocompatibility and safety, as well as limitations in resolution to achieve extremely fine features in the design of sophisticated microneedles. Post-processing requirements such as cleaning and curing make the manufacturing process more complex and time-consuming. Despite these drawbacks, technological developments can solve these problems, and the suitability of SLA depends on the specific requirements of the microneedle application and the desired characteristics of the final product (Economidou and Douroumis, 2021; Khurana et al., 2013).

One of our aims was to enhance lidocaine delivery, so we explored the development of an NLC system, as a passive permeation enhancer, using a 2^3 full factorial design. Our focus was on characterizing the stable drug carrier system formulated for dermal use, comparing it with a traditional dermal ointment in terms of physicochemical and biopharmaceutical properties. Furthermore, we investigated the influence of 3D printed solid microneedles, acting as active permeation enhancers, on the biopharmaceutical properties of the systems. By actively promoting drug permeation through the skin, microneedles can complement the passive transport achieved by NLCs, offering an innovative and synergistic approach to improving lidocaine delivery.

2. Materials and methods

2.1. Materials

Lidocaine and macrogol 400 were obtained from Hungaropharma Ltd. Apifil ® (PEG-8 Beeswax) was provided by Gattefossé (St. Priest Cedex, France). Miglyol® 812 (caprylic/capric triglyceride) was from Sasol GmbH (Hamburg, Germany). Kolliphor® RH40 (PEG-40 hydrogenated castor oil) was kindly supplied by BASF SE Chemtrade GmbH (Ludwigshafen, Germany). Acetonitrile (high-performance liquid chromatography [HPLC] grade), and H_3PO_4 (85 %) (analytical grade) were purchased from VWR Int Ltd (Radnor, PA, USA). Carbopol 971P NF was supplied by Azelis Ltd (Budapest, Hungary). Purified water (HPLC grade) produced with a TKA Smart2Pure system (TKA GmbH, Niederelbert, Germany) was used to prepare all the formulations. Purified and deionized water was used (Milli-Q system, Millipore, Milford, MA, USA). High Temp V2 resin (Formlabs, Somerville, Massachusetts, USA) was obtained from Dental Plus Kft. (Sopron, Hungary). Isopropyl alcohol (IPA) was acquired from Molar Chemicals (Halásztelek, Hungary). Human skin was acquired from a Caucasian female patient who underwent an abdominal plastic surgery procedure at the University of Szeged, Department of Dermatology and Allergology. The investigations were performed with the approval of the Hungarian Medical Research Council (ETT-TUKEB, registration number: BMEÜ/2339–3/2022/EKU).

2.2. Methods

2.2.1. Preparation and characterization of the NLC system

2.2.1.1. Preparation of lidocaine-loaded NLC. The lidocaine-loaded NLC was prepared using the high shear homogenization method, more specifically probe sonication (Fig. 2) (Zsikó et al., 2019). Lidocaine was dissolved in a mixture of molten solid lipids (Apifil), liquid lipid (Mygliol 812 N) and surfactant (Kolliphor RH 40). The bulk mixture was melted at 80 °C under controlled stirring, with the temperature maintained 10 °C above the melting point of the solid lipid (Apifil), at approximately 80 °C, to hinder recrystallization. The aqueous phase, containing purified water, was heated to its boiling point, and then poured into the lipophilic phase to create a pre-emulsion. In order to break down large lipid droplets, the pre-nano emulsion underwent ultrasonication using a Hielscher UP200S compact ultrasonic homogenizer (Hielscher Ultrasonics GmbH, Teltow, Germany) for 10 min at 70 % amplitude. Finally, the sample was rapidly cooled in an ice bath at 0 °C or in a water bath at room temperature (25 °C) to stabilize the NLC formulations. Subsequently, they were placed in a glass container and stored in a refrigerator (Shimojo et al., 2019).

Table 1
Compositions of NLC formulations.

Sample	Lidocaine w/w%	Kolliphor RH40 w/w%	Apifil/ Miglyol 812 w/w%	Purified Water w/w%	Cooling process (°C)
NLC 1	1	1	6/4	up to 100	0
NLC 2	1	1	6/4	up to 100	25
NLC 3	1	5	6/4	up to 100	0
NLC 4	1	5	6/4	up to 100	25
NLC 5	2	1	6/4	up to 100	0
NLC 6	2	1	6/4	up to 100	25
NLC 7	2	5	6/4	up to 100	0
NLC 8	2	5	6/4	up to 100	25

Table 2
Experimental design, values, and levels of independent variables.

Determinants	Code	Lower level (−1)	Upper level (+1)
Independent			
Lidocaine (w/w) %	(X_1)	1	2
Surfactant (w/w) %	(X_2)	1	5
Temperature of Cooling Process (°C)	(X_3)	0	25
Dependent Variables			
Zeta Potential (mV)	(y_1)		
Particle Size (nm)	(y_2)		
Encapsulation Efficiency (%)	(Y_3)		

The solid lipid/liquid lipid ratio was 6:4 in all preparations.

2.2.1.2. Design of experiments (DoE). Based on the literatures (Fudin et al., 2020; Pathak and Nagarsenker, 2009; Reddy and Gubbiyappa, 2022; Zsikó et al., 2019), the concentration of the active pharmaceutical ingredient (API) (1–2 %), the amount of surfactant (1–5 %) and the cooling process (0–25 °C)were the chosen critical factors in the formulation of NLCs containing lidocaine. Using a 2^3 factorial design, eight different formulations were prepared, and the most effective formulation was chosen for further analysis.

The composition of eight NLC formulations containing lidocaine with two levels of each factor was prepared according to a 2^3 full factorial experiment, as shown in Table 1.

To investigate the interaction and influence of the experimental conditions (independent variables) on dependent variables, 8 samples were prepared by employing the 2^3 factorial design approach. The optimization of three independent variables, such as the effects of lidocaine (X_1) and surfactant (X_2) concentration, and cooling process temperature (X_3), and the interaction between them were evaluated for each dependent variable, zeta potential (y_1) particle size (y_2) and encapsulation efficiency (%) (Y_3). Lower (−1) and upper level (+1) values of x1, x2, and x3 are presented in Table 2.

2.2.2. Characterization of the NLC system

2.2.2.1. Measurement with differential scanning calorimetry (DSC). The melting behaviour and crystallinity state (crystallinity index) of the components as well as the physical mixture of the components were evaluated with a DSC (Mettler-Toledo 821e DSC instrument (Mettler-Toledo GmbH, Greifensee, Switzerland) thermal analysis system with the STARe thermal analysis software version 16.30. Assays were performed using a 40-μL covered aluminum sample holder with 2 holes. An empty aluminum pan was used as the reference. The weight of our test

samples ranged from 2 to 5 mg in each case, and the data were normalized to the weight of the sample. During the tests, the heating rate was 5 °C/min, under a 40 mL/min constant flow of nitrogen gas as the carrier purge gas. In our studies, we used temperature ranges (10–100 °C).

For the measurements, the ratio of the components in the physical mixtures was solid lipid: liquid lipid: surfactant: lidocaine 6:4:1:2. The lipid compositions were melted, and lidocaine was added and mixed with a magnetic stirrer at about 100 rpm (Stuart CB162 magnetic stirrer, Merck, Germany) until complete dissolution and then cooled (Sütő et al., 2015). From the results of the DSC measurements, the crystallinity index (CI%) of the lipid compositions was calculated with Eq (1):

$$\frac{\Delta H\text{bulk material} \times \text{solid lipid ratio}}{\Delta H\text{solid lipid}} \times 100 = CI(\%) \quad (1)$$

2.2.2.2. Measurement with X-ray diffractometry (XRD). The crystalline structure of a physical bulk mixture of the components was characterized with XRD using a BRUKER D8 Advance diffractometer (Bruker AXS GmbH, Karlsruhe, Germany) equipped with Cu K λ I radiation (λ = 1.5406 Å) and a VANTEC 1 detector. The samples were scanned at the voltage of 40 kV and the amperage of 40 mA. The angular range was 3° to 40°, 2θ with a step time constant of 0.1°/s, and a step size of 0.0073°. The manipulations and evaluations were carried out using EVA Software (EVA Software Solutions, A223, Mumbai, India).

The preparation of the physical mixtures for XRD followed the DSC procedure, while the samples for the NLC formulations were prepared through lyophilization. Freeze-drying was applied with a Scanvac CoolSafe laboratory freeze-dryer (Labogene, Lynge, Denmark) at − 40 °C for 24 h under a pressure of 0.015 mbar, with an additional 4 h of secondary drying at 22 °C. The lyophilized powder was stored at 5 ± 3 °C for further investigations.

2.2.2.3. Dynamic light scattering (DLS) and zeta potential measurements. The particle size, expressed as the average hydrodynamic diameter (Z-average), the zeta potential (ZP), and the polydispersity index (PDI) of the NLC formulations were measured using the DLS technique with a Malvern Zetasizer Nano ZS system (Malvern Panalytical Ltd., Malvern, Worcestershire, UK). The measurements were conducted at 25 °C with a 633 nm wavelength laser, using 1 mL of sample in a folded capillary cell, and a refractive index of 1.36. The NLCs were diluted 20-fold with purified water. Three parallel measurements were carried out (n = 3), and the results were expressed as the mean ± standard deviation (S.D.).

2.2.2.4. Measurement of encapsulation efficiency and drug loading. Encapsulation efficiency (EE) and drug loading capacity (DL) were measured using the indirect method (Uprit et al., 2013). A fixed volume (2 mL) of the NLCs was prepared and centrifuged employing a Hermle Z323K high-performance refrigerated centrifuge (Hermle AG, Gossheim, Germany) at 10,000 rpm and 5 °C for 25 min, in a centrifuge tube mounted with an ultrafilter (Vivaspin 15R 5000 MWCO Hydrosart tubes (Sartorius, Stonehouse, UK). After that, the amount of free lidocaine in the supernatant was determined using HPLC (Shimadzu Nexera X2 UHPLC, Kyoto, Japan), equipped with a C18 reverse-phase column (ZORBAX Eclipse XDB-C18, Phenomenex, Torrance, CA, USA) with 5 μm, 4.6x150 mm dimension. The mobile phase was 0.1 % phosphoric acid (solvent A): acetonitrile (solvent B) 90:10 in gradient mode. It was changed from 90:10 (A:B, v/v) to 40:60 (A:B, v/v) in 6 min, and then back to 90:10 (v/v) between 6.1 and 10 min. The flow rate of 0.8 mL/min was set over 10 min, the column temperature and sample tray temperature were set to 25 °C, and the detection was made at 230 nm. The injection volume was 5 μL. The time of analysis was 10 min, and the retention time was 4.2 min.

Encapsulation efficiency (EE%) was calculated using the following Eq. (2).

$$EE\% = \frac{W_{\text{initial drug}} - W_{\text{free drug}}}{W_{\text{initial drug}}} \times 100\,\% \quad (2)$$

Drug loading capacity (DL%) was calculated using the following Eq. (3).

$$DL\% = \frac{W_{\text{initial drug}} - W_{\text{free drug}}}{W_{\text{lipid}}} \times 100\,\% \quad (3)$$

where $W_{\text{initial drug}}$ is the weight of total drug in the NLC, while $W_{\text{free drug}}$ is the weight of free drug detected in the filtrate, while W_{lipid} is the weight of lipids in the formulations in micrograms.

2.2.3. Preparation of dermal formulations

2.2.3.1. Preparation of ointment. According to the official Hungarian pharmaceutical book (FoNo VIII), the ointment was prepared containing Macrogol (polyethylene glycol) 400 and 1500 in a ratio of 1:1 with 2 % (w/w) lidocaine, which serves as a reference formulation. First, the ointment base was melted at a temperature of 60–70 °C, then lidocaine was added to the melted base and the mixture was stirred until cooling. This process ensures that lidocaine is evenly distributed within the ointment base, resulting in a consistent ointment texture. The blank ointment was also prepared in the same way, without adding lidocaine.

2.2.3.2. Preparation of NLC gel. In order to compare our optimized NLC system (NLC 6), which was selected based on the results of our experimental design) with the conventional ointment, we jellified the outer phase of our NLC system to make it applicable on the skin. Carbopol 971P NF was used as a gelling agent to incorporate the outer phase of the NLC, to enhance viscosity, and to ensure topical application and skin adhesion. First, the concentrated NLC was prepared (reducing the water content). Then, Carbopol 971P NF polymer was slowly sprinkled into the purified water (remaining from the NLC composition) and dispersed by stirring. The pH was adjusted with the dropwise addition of trolamine to the system to create the gel structure. Finally, the concentrated NLC and the polymer solution were mixed until a homogenous texture was obtained. The final concentration of the gelling agent was 1 % (w/w).

2.2.4. Rheological measurement of dermal preparations

The rheological measurements were carried out with a Physica MCR301 rheometer (Anton Paar GmbH, Graz, Austria) to investigate the properties of the semisolid preparations and the effect of lidocaine on the rheological parameters. Parallel plate geometry CP25 was applied with a measuring gap of 0.1 mm. The blank formulations were also studied. Flow curves and viscosity parameters were obtained during the examination. The shear rate was raised from 0.1 to 100 1/s (up-curve) and then reduced from 100 to 0.1 1/s (down-curve) in CR mode. The shearing time was 300 s and the measurements were made at 25 °C. The viscosity values were obtained at a shear rate of 50 1/s (Zsikó et al., 2019).

2.2.5. Preparation of 3D printed microneedle arrays

3D models of the microneedle arrays (MNAs) were designed with Shapr3D (Shapr3D, Budapest, Hungary) software. The final design contained 8x8 conical needles with a needle height of 1 mm on a carrier of 7.2x7.2x1 mm. Subsequently, the MNA models were imported into Preform (Formlabs, Somerville, Massachusetts, USA) software and prepared for printing. The MNAs were printed with High Temp V2 resin at a layer height of 25 μm on a Formlabs Form 3 (Formlabs, Somerville, Massachusetts, USA) SLA printer. The post-processing of the printed samples was performed along the following steps: mixing for 6 min in IPA in a beaker with a magnetic stirrer. Drying was performed with compressed air. The end-polymerization step was done in a Form Cure (Formlabs, Somerville, Massachusetts, USA) heated UV chamber at 80 °C for 2 h. The final MNAs were applied in the experiments described below.

2.2.6. Characterization of 3D printed microneedle array and penetration into the skin by confocal fluorescence microscopy

The MNAs, prepared according to Section 2.2.5., were immersed in liquid oil labelled with curcumin dissolved in Miglyol 812. This mixture was used as a fluorescent substrate to colour the MNAs, enabling visualization under the confocal fluorescence microscope. The excised abdominal human full skin was used for the microscopic visualization of the penetration of the microneedle into the skin. The skin was punctured by MNAs using an A.XT plus Texture Analyzer with a 10-mm-diameter cylinder probe. (Stable Micro Systems Ltd., Surrey, UK). The MNAs were fixed on the probe and the system was inserted into the skin under controlled circumstances (insertion force: 30 Newton; holding time in the epidermis: 30 s).

A Leica DMI 8 – Stellaris 5 laser scanning confocal microscope system equipped with Leica Application Suite X and Leica 3D Viewer software was used for imaging and 3D reconstruction (Leica, Heidelberg, Germany). A 448-nm excitation laser at 10 % intensity was used for curcumin excitation. Emission was detected using a spectral HyD detector between 462 and 749 nm. HC PL Fluotar 5x (N.A. 0.15) and HC PL Fluotar 10x (N.A. 0.30) dry objectives were used to capture 126 and 100 optical sections, respectively. Composite images were prepared using the CorelDraw graphics suite X7 (Corel, Ottawa, Canada) software.

2.2.7. Biopharmaceutical investigations

To compare the biopharmaceutical profile of the NLC gel, ointment alone and assisted with microneedle, Franz diffusion cell and Raman spectroscopy were used.

2.2.7.1. In vitro release profile and skin permeation studies. In vitro drug release (IVRT) and *in vitro* drug permeation (IVPT) were evaluated with a Franz diffusion cell (Phoenix RDS automatic diffusion system, Teledyne LABS, Thousand Oaks, CA, USA). It was designed with a donor and an acceptor phase, which were separated by either a synthetic cellulose acetate membrane or heat-separated human epidermis (HSE). The cellulose membrane (Porafil membrane filter, cellulose acetate, pore diameter: 0.45 μm, (Macherey-Nagel GmbH & Co. KG (Düren, Germany)) was soaked for a few minutes in freshly prepared phosphate buffer (PBS, pH = 7.4). The HSE, which was supported by a synthetic membrane on mounted of cells, was prepared after it was placed in a water bath (60 ± 0.5 °C) and then the epidermis was separated from the dermis. A volume of approximately 0.3 g of the semisolid formulations was placed on the membrane. The acceptor chamber, containing 10 mL of PBS, was kept at 32.5 °C with a stirring speed of 400 rpm. In the case of IVRT, the experiment lasted for 6 h in the six parallel cells (sampling times: 0.5; 1; 2; 4; 5; 6 h). In the case of IVPT, the experiment ran over 24 h in the six parallel cells (sampling times: 0.5; 1; 2; 3; 4; 5; 6; 8; 10; 12; 16; 20; and 24 h). The cumulative amount of lidocaine in the receptor phase was analysed by HPLC, according to the method described in Section 2.2.2.4. The same procedure was repeated to evaluate the *in vitro* drug permeation study of both formulations after the HSE membrane was pretreated with 3D printed MNAs. The A.XT plus Texture Analyzer (Stable Micro Systems Ltd., Surrey, UK) was used to insert the microneedle uniformly into the skin samples. This method was described in Section 2.2.5. The formulations were then applied to the pretreated epidermis, and the further procedure was the same as previously described.

According to the EMA guideline (EMA, CHMP/QWP/708282/2018), IVRT is a useful method to evaluate the rate and extent of the release of the active substance in both formulations. The following parameters were determined: a., drug release rate, which is the slope of the cumulative amount of the active substance released versus the square root of time for the linear portion of the drug release profile; b., the cumulative amount of the active substance released, expressed in mass units per surface area, at the last sampling time of the linear portion.

Table 3
Melting point peaks (°C) and crystallinity index CI (%) of pure Apifil, the lipid mixture in a ratio of (6:4), and the lipid mixture with Kolliphor RH40 in a ratio of (6:4:1) and with the addition of lidocaine in a ratio of (6:4:1:2), and NLC formulations.

Sample	(Transition 1) (°C)	(Transition 2) (°C)	CI (%)
Apifil	51.15	61.11	100
Apifil: Miglyol 812 (6:4)	44.79	55.20	34.62
Apifil: Miglyol 812: Kolliphor RH40 (6:4:1)	43.23	54.23	23.44
Apifil: Miglyol 812: Kolliphor RH40: lidocaine (6:4:1:2)	44.03	55.37	21.13
NLC Blank	45.18	52.18	37.12
NLC + Lid	44.04	52.21	27.45

2.2.7.2. Raman spectroscopy. The excised human full skin was also used for Raman mapping. The skin samples were placed on filter papers soaked with PBS and a 2-cm surface of the skin was cut. Subsequently, the skin samples were treated for 3 h with NLC gel and blank ointment, with both formulations containing lidocaine. Additionally, the skin was pretreated with a 3D printed microneedle (using A. XT plus Texture Analyzer (Stable Micro Systems Ltd., Surrey, UK), with the method described in the previous Section), followed by the application of two semisolid formulations with and without lidocaine. After the treatment, any residue from the formulations was removed. Subsequently, a strip line was cut from the treated skin, and it was then transferred to the Leica CM1950 Cryostat (Leica Biosystems GmbH, Wetzlar, Germany). 15-μm-thick cross-sections were prepared and placed on aluminum-coated slides for Raman spectroscopy using a Thermo Fisher DXR Dispersive Raman Spectrometer (Thermo Fisher Scientific Inc., Waltham, MA, USA) equipped with a CCD camera.

The spectra of lidocaine and the semisolid formulations (NLC gel and ointment) with or without lidocaine were collected with laser light of 780 nm with an exposure time of 6 s, with 24 scans, including cosmic ray and fluorescence corrections. The measurements were carried out with a laser power of 10 mW at a slit width of 25 μm.

The localization of lidocaine in the skin sections by employing Raman mapping was conducted with laser light of 780 nm as the excitation source, which provides sufficient energy for vibrations in skin proteins. The laser power focused on the sample was set to 24 mW, which can be considered non-destructive for biological samples but effective for the samples in these studies (Tfayli et al., 2007). The measurements were captured using a 50x objective lens. Throughout the mapping process, a skin area of 100 × 500 μm was imaged with a vertical and horizontal step size of 50 μm. The map of untreated skin was used as a control during the measurement. 24 spectra were captured in each point and measurements were carried out. The OMNIC™ 8.2 for Dispersive Raman software package (Thermo Fisher Scientific Inc., Waltham, MA, USA) was used for both data acquisition and analysis.

2.2.7.3. Statistical analysis. Statistical data analysis was performed using Prism for Windows software (GraphPad Software Inc., La Jolla, CA, USA). The statistical difference between samples was analysed using two-way ANOVA followed by the Bonferroni post-test.

Levels of $p \leq 0.05$*, $p \leq 0.01$** and $p \leq 0.001$*** were significant versus the control. Six parallel measurements were conducted for IVRT and IVPT (L. Kiss et al., 2019).

3. Results and discussion

3.1. Characterization of the NLC system

3.1.1. Results of DSC measurements

The results of DSC measurements play a crucial role in characterizing the degree of lipid crystallinity and the modification of lipid behaviour,

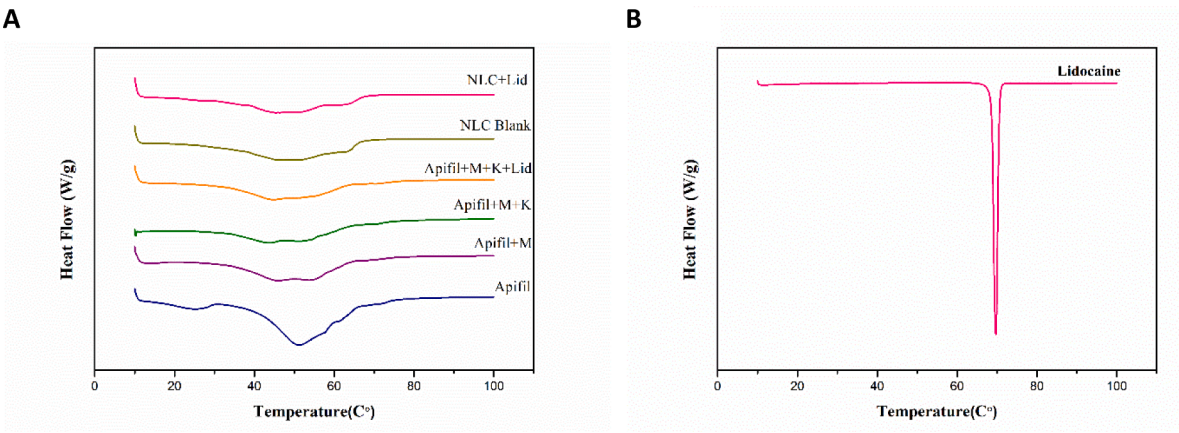

Fig. 3. **A**: DSC curves of pure Apifil and bulk mixtures of Apifil with the addition of Miglyol 812 (Apifil + M), further addition of Kolliphor RH40 (Apifil + M + K), additional lidocaine (Apifil + M + K + Lid), lidocaine-free NLC (NLC Blank) and NLC loaded with lidocaine (NLC + Lid); **B**: DSC thermogram of lidocaine.

which significantly affect the performance of NLC carriers. These parameters are closely linked to the incorporation and release rates of the drug (Sütő et al., 2015).

Table 3 lists the melting point peaks (°C), and the CI% of pure Apifil, the 6:4 bulk lipid mixture, and the bulk lipid mixture with surfactant, then with lidocaine in a ratio of 6:4:1 and 6:4:1:2 respectively and finally lyophilized NLC with and without API. The CI% was calculated based on Eq. (1), showing a decrease from 100 % to 21.13 % with the addition of Miglyol 812 and the incorporation of surfactant and API into the bulk lipid matrix (Uprit et al., 2013).

Apifil, an ester derivative of long-chain fatty acids and a monohydric alcohol chain of beeswax with a polyethylene glycol (PEG) group, imparting hydrophilic properties to beeswax (Tulloch, 1970), displayed a broad endothermic event with a glass transition at 26.1 °C and 2 melting points at 51.15 °C and later at 61.11 °C.

Miglyol 812, a triglyceride ester of saturated coconut/palm kernel oil derived from caprylic and capric fatty acids and plant-derived glycerol, interacts with Apifil and influences the overall thermal behavior observed in the DSC thermogram (Fig. 3). This interaction leads to the disappearance of the glass transition state in Apifil and shifts the two melting point peaks at 44.79 °C and 55.20 °C with a broader endothermic event.

In addition, lipid matrices are less crystalline than the individual components used in the formulation due to their lower enthalpy values. This means that there is a distortion in the crystal arrangement of the lipids after melting and solidification, which generates an imperfect matrix, thus leaving spaces for drug encapsulation in the NLCs and improving drug loading capacity.

With the addition of surfactants and lidocaine to Apifil and Miglyol 812, the melting peaks also broadened and decreased in height, which could be attributed to the dispersion of lidocaine in the physical mixture of components, significantly increasing the formation of imperfect lattices and the distortion of the crystallinity of Apifil. It allows the matrix of the NLCs to accommodate a greater amount of lidocaine.

The thermal curve of NLCs showed the appearance of a shoulder peaked at about 62 °C after the major endothermic peaks and exhibited higher crystallinity indexes compared to bulk mixtures with the same compositions. It may be caused by recrystallization of the lipid as a result of the lyophilization process of NLCs before DSC measurements (Kovacevic et al., 2011). Additionally, the DSC thermograms of the NLCs revealed a similar pattern, however, the NLC Blank expressed a wider endothermic melting peak and higher crystallinity compared to lidocaine loaded NLC, similar to the results of bulk mixtures.

3.1.2. Results of XRD analysis

The samples were prepared in the same manner as before for the DSC measurements. The diffraction pattern of the analysed materials was assessed using the XRD method. Lidocaine has a very sharp and exact crystalline structure, and a partial crystalline nature can be found in the diffractogram of Apifil, which is repeated in all mixtures (Fig. 4) (Tetyczka et al., 2019).

The characteristic peaks of lidocaine were absent in all examined samples. This suggests that lidocaine was uniformly and molecularly

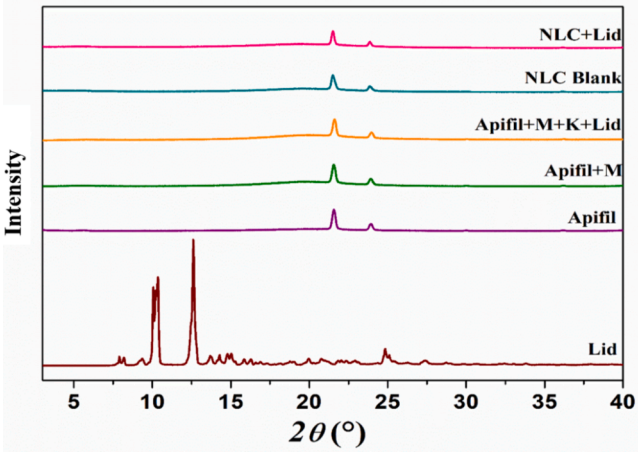

Fig. 4. XRD diffractogram of raw material lidocaine (Lid) and Apifil, physical mixture of Apfil and Miglyol 812 (Apifil + M), physical mixture of Apifil, Miglyol 812 and Kolliphor RH40, physical mixture of Apifil, Miglyol 812, Kolliphor RH40 and lidocaine (Apifil-M−K−Lid), and NLC without lidocaine (NLC Blank), and NLC with lidocaine (NLC + Lid).

Table 4
Particle size, polydispersity index, and surface charge of lidocaine-loaded NLC formulations. Results are presented as the mean ± S.D. (n = 3).

Sample	Z- Average (nm)	PDI	Zeta Potential(mV)
NLC 1	236.4 ± 2.230	0.217 ± 0.009	−60.56 ± 2.402
NLC 2	237.56 ± 0.650	0.191 ± 0.017	−41.56 ± 0.41
NLC 3	82.45 ± 0.273	0.196 ± 0.008	−39 ± 0.88
NLC 4	67.97 ± 0.49	0.138 ± 0.024	-33.76 ± 0.50
NLC 5	254 ± 2.40	0.183 ± 0.014	−54.43 ± 1.72
NLC 6	255.66 ± 1.90	0.225 ± 0.009	−44.06 ± 1.06
NLC 7	69.77 ± 0.32	0.134 ± 0.010	−34.9 ± 8.33
NLC 8	68.71 ± 0.23	0.117 ± 0.011	−44 ± 2.77

Table 5
Encapsulation efficiencies (EE%) and Drug Loading (DL%) in NLCs.

Sample	EE%	DL%
NLC 1	79	7.9
NLC 2	79.77	7.97
NLC 3	68.53	6.85
NLC 4	95.15	9.51
NLC 5	67.6	13.52
NLC 6	94.51	18.90
NLC 7	48.79	9.75
NLC 8	62.75	12.55

Table 6
Relationship between the composition of independent variables X_1, X_2, X_3 and the dependent variables of the NLCS, such as zeta potential (Y_1), particle size (Y_2), and encapsulation efficiency (Y_3).

Sample	(X_1) Lidocaine (w/w) %	(X_2) Surfactant (w/w) %	(X_3) Cooling Process	(Y_1) Zeta Potential (mV)	(Y_2) Particle Size (nm)	(Y_3) EE %
NLC 1	1(−1)	1(−1)	0(−1)	−60.57	236.47	79
NLC 2	1(−1)	1(−1)	25(+1)	−41.57	237.57	79.7
NLC 3	1(−1)	5(+1)	0(−1)	−39	82.46	68.5
NLC 4	1(−1)	5 (+1)	25(+1)	–33.77	67.98	95.1
NLC 5	2(+1)	1(−1)	0(−1)	−54.43	254	67.6
NLC 6	2(+1)	1(−1)	25(+1)	−44.07	255.67	94.5
NLC 7	2(+1)	5(+1)	0(−1)	−34.9	69.78	48.7
NLC 8	2(+1)	5(+1)	25(+1)	−44	68.72	62.7

dispersed in both the NLC and the bulk mixture of all components. It is to be noted that two partial peaks can be seen at the 2Θ value of around 20-25° in the X-ray scan of all physical mixtures and freeze-dried NLCs formulations, which is one of the peaks characteristic of Apifil, implying that the partial crystallinity pattern of Apifil is preserved in the NLC formulations (Pathak and Nagarsenker, 2009).

3.1.3. Results of particle size characterization and zeta potential measurements

The typical diameter of traditional NLCs ranges between 10 to 1000 nm, although a preferred size range of 50–300 nm interval is desired for site-specific drug release (Müller et al., 2000). One of the most important advantages of these lipid nanostructured carriers is higher permeability, which improves uptake, rapid action, and controlled release. The average size of both blank and lidocaine-loaded NLCs was below 300 nm, between 67.97 and 255.66 nm (Table 4). The PDI was found to be lower than 0.3, indicating a monodisperse distribution and relative uniformity in the final NLC preparations. The NLC surface charge revealed high negative values between –33.76 and −60.56, which is required for excellent and good physical stability. This characteristic is attributed to the chemical composition of the lipid matrix and the presence of surfactant (Kolliphor RH40), which stabilizes the system.

3.1.4. Results of encapsulation efficiency and drug loading

The percentage of the drug incorporated in the lipid matrix (encapsulation efficiency and drug loading) was evaluated by an indirect method, with the measurement of the free drug concentration in the

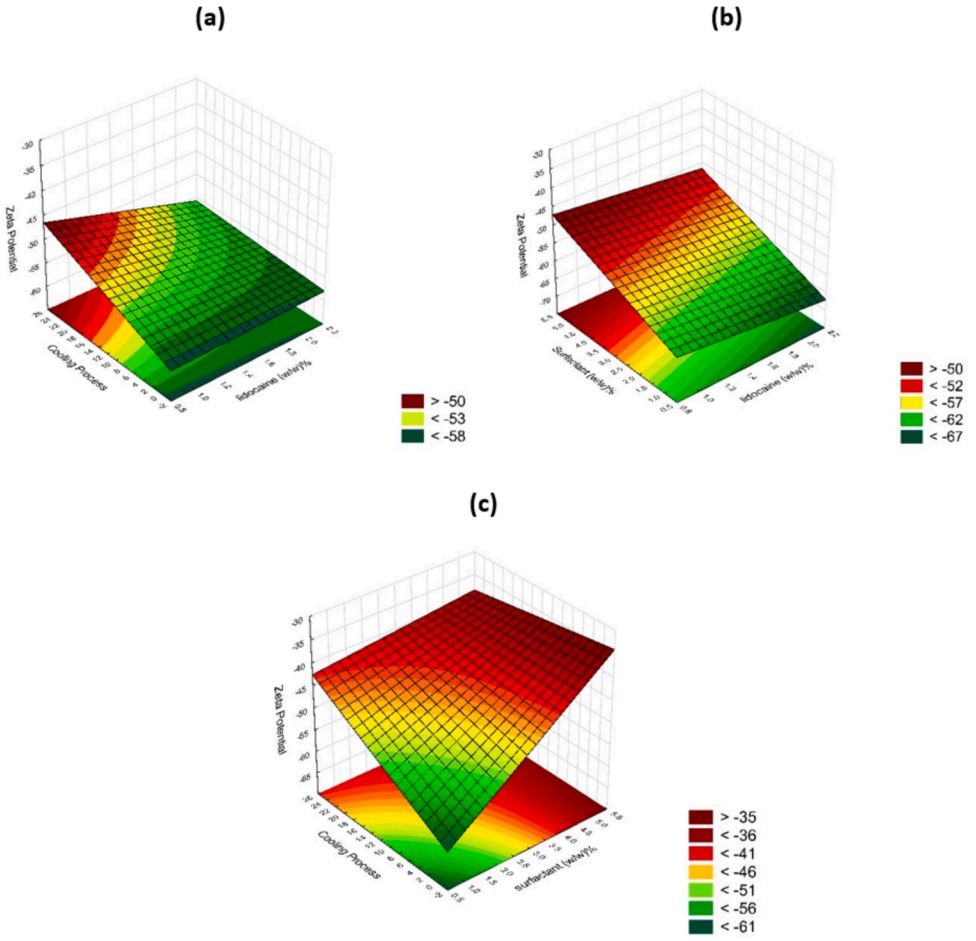

Fig. 5. Effect of the compositions and the cooling process on zeta potential: (**a**) cooling process and lidocaine concentrations, (**b**) surfactant and lidocaine concentrations, (**c**) cooling process and surfactant.

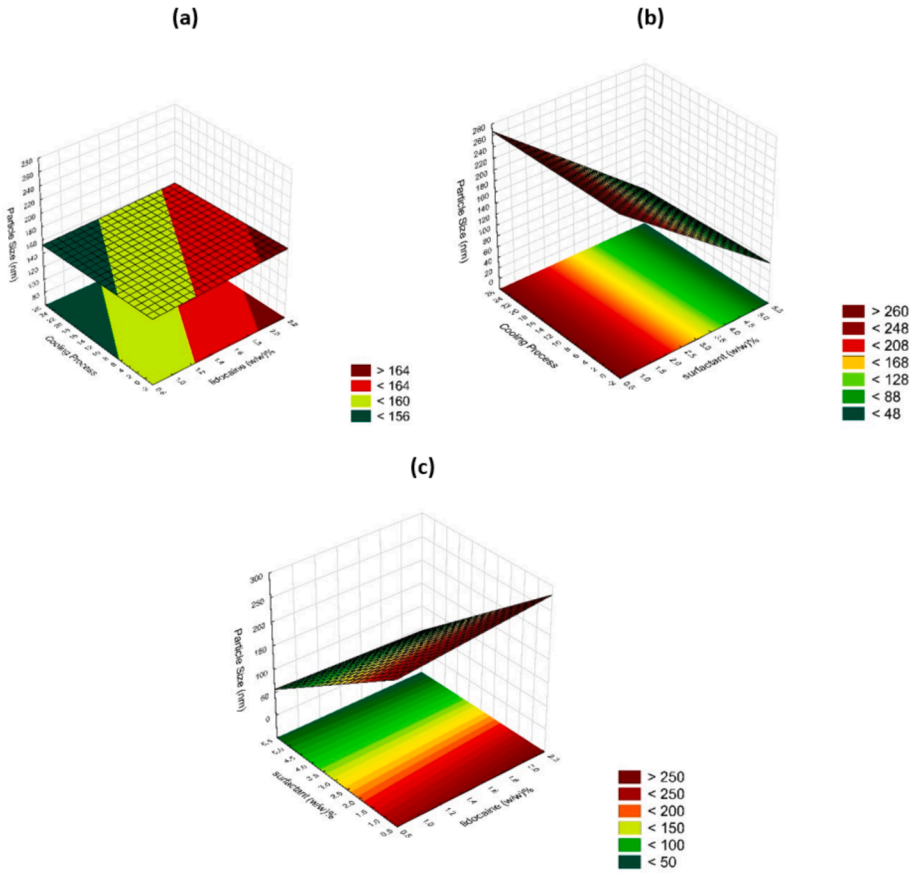

Fig. 6. Effect of the composition on particle size: (**a**) cooling process and lidocaine concentrations, (**b**) cooling process and surfactant concentrations, (**c**) surfactant and lidocaine.

external aqueous phase. The encapsulation efficiency and drug loading capacity of lidocaine within the NLCs was quantified using a validated HPLC analytical method, as described in 2.2.2.4. All tested NLC formulations exhibited high encapsulation efficiencies and drug loadings, suggesting the successful encapsulation of lidocaine within the lipid nanoparticles (Chauhan et al., 2020) (Table 5).

3.1.5. Analysis of the results of DoE

In order to find the optimum formulation, an eight-run 2^3 factorial design was implemented and executed (Table 6). The Statistica for Windows (version 13.5, Stat Soft Inc., Tulsa, OK, USA) program was applied to compare and analyse the optimized effect on responses. The confidence interval was 95 %, and the alpha value indicating significant factors was 0.05 %. The unnecessary determinants were eliminated from the equations to increase the fitting accuracy by maximizing the adjusted R^2 values, where Y is the response parameter for each factor level; β0 is an intercept, −1, +1 are the coded levels of the independent variables. Eq. (4) was used to determine the coefficients, and the positive and negative mathematical signs imply a synergistic effect and an antagonistic effect. A multiple linear regression analysis was performed to estimate the effect of factors on responses by generating a polynomial equation (Preethi et al., 2022):

$$Y = \beta_0 + \beta_1 A + \beta_2 B + \beta_3 C + \beta_{12} AB + \beta_{23} BC + \beta_{13} AC + \beta_{123} BC \quad (4)$$

To identify the best-fit model, the results were subjected to several regression models: Linear, Two-Factor Interactions (2FI) and Three-Factor Interactions (3FI) in the design of experiments. Based on the Adjusted Squares (Adj value) and MS Residual value, the best-fit significant model for all the responses was analysed and presented by the equations, as shown in Eqs.5–7.

The best equation for zeta potential was obtained after ignoring X_1 (lidocaine concentration) and X_1 X_2 X_3 interaction factors. The surfactant concentration and the cooling process were significant factors regarding zeta potential (Y_1), (Eq. (5) (Fig. 5).

$$Y_1 : -44.0388 + 6.1213X_2 + 3.1863X_3 - 1.2212\ X_1X_2 - 2.8712X_1X_3 - 4.1538X_2X_3 \quad (5)$$

The best equation for particle size was obtained after ignoring X_3 (cooling process) factor, with Adjusted square number of 0.99765 and Ms residual of 20.38411. Surfactant concentration X_2 exhibited significant factor and the X_1 X_2 interaction was the factor with highest coefficient (Eq. (6) (Fig. 6).

$$Y_2 : 159.0813 + 2.9613\ X_1 - 86.8462X_2 - 5.9463\ X_1X_2 + 1.7487\ X_1X_3 - 2.2887\ X_2X_3 + 1.6062\ X_1X_2X_3 \quad (6)$$

The best equation for encapsulation efficiency was obtained with a 3-factor interaction after ignoring the X_2 X_3 interaction, with Adjusted square number of 0.91713 and MS Residual of 20. 80125. Although this equation did not reveal any significant factor, the effect of the cooling temperature was the greatest value and can be visualized by the surface plot.. After ignoring the X_1 X_3 interaction, the cooling process showed a significant effect with lower Adjusted square number: 0.91332 and higher MS Residual: 21.75753, (Eq. (7) (Fig. 7).

$$Y_3 : 74.51250 - 6.10000\ X_1 - 5.70750\ X_2 + 8.53250\ X_3 - 6.93500\ X_1X_2 + 1.68500\ X_1X_3 - 4.85000\ X_1X_2X_3 \quad (7)$$

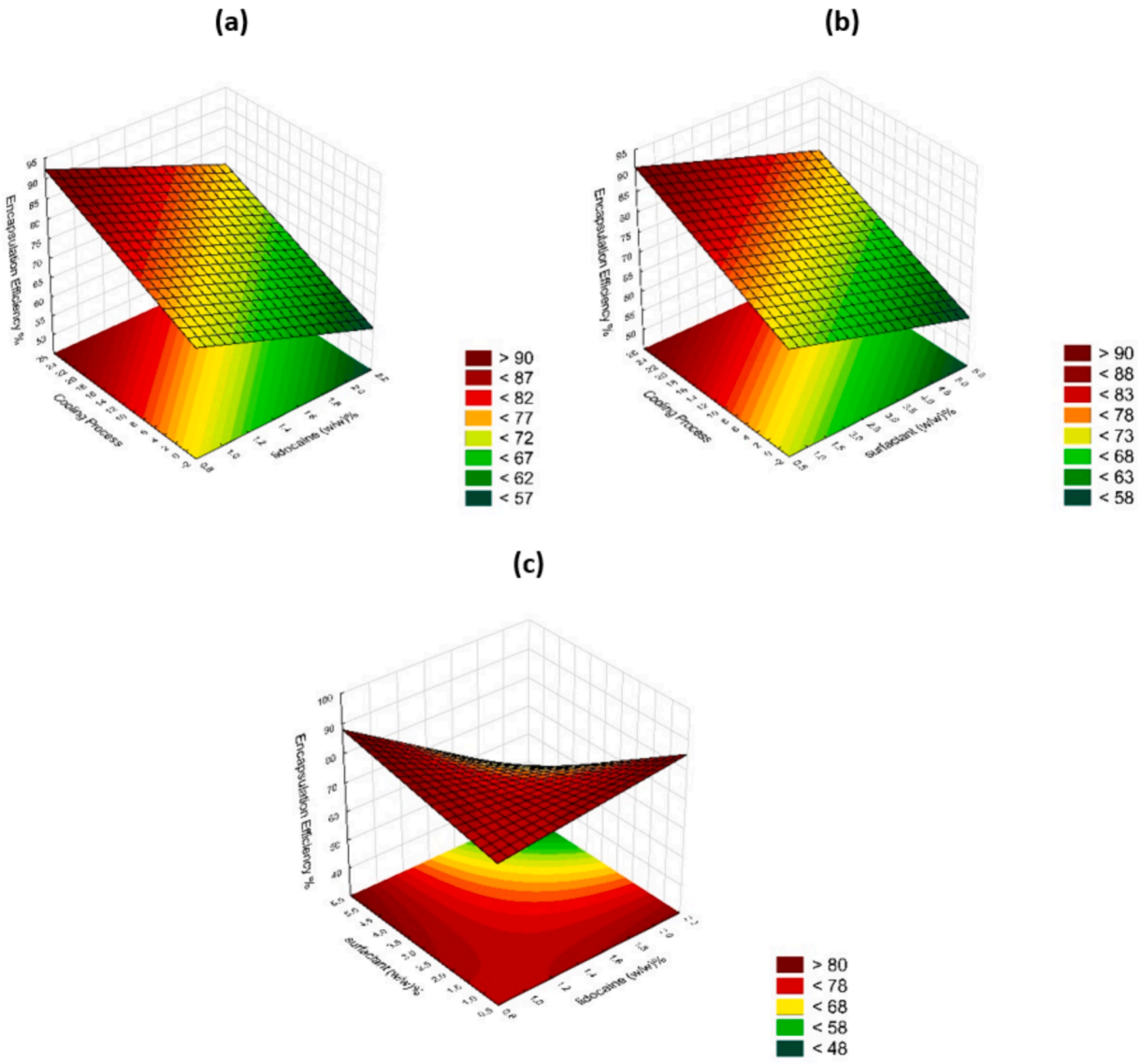

Fig. 7. Effect of the composition on encapsulation efficiency: (**a**) cooling process and lidocaine concentrations, (**b**) cooling process and surfactant concentrations, (**c**) surfactant and lidocaine.

The best-fit models were determined based on Adjusted Squares and MS Residual values for each response parameter. The results indicated that surfactant concentration and cooling process significantly influenced zeta potential, while surfactant concentration and their interaction were significant for particle size. Increasing surfactant concentration caused a reduction in particle size and the absolute value of zeta potential, while a lower cooling temperature (0 °C) resulted in higher zeta potential values. Our result agreed with the work of Witayaudom, and Klinkesorn (Witayaudom and Klinkesorn, 2017). In case of encapsulation efficiency, there was no significant factor, although the cooling process showed the highest coefficient, indicating that a higher cooling temperature of 25 °C resulted in higher encapsulation efficiency. Lidocaine concentrations had no significant effect on the dependent parameters.

It was concluded that optimizing these factors can enhance the characteristics of NLCs containing lidocaine for potential applications in dermal therapeutics and aesthetic procedures. Based on this evaluation, we selected sample NLC 6 (2 % lidocaine, 1 % Kolliphor RH 40, cooling process: room temperature at 25 °C), with a zeta potential of −44 mV, a particle size of 255 nm, and encapsulation efficiency of 94 % for further investigation. All the data generated by the software and the adjustments are presented in the supplementary material (S1).

3.2. Results of the rheological measurement of semisolid dermal preparations

The rheological analysis of both the blank and lidocaine-loaded NLC gels exhibited very slight thixotropy with a yield stress of 34–50 Pascal. NLC gels showed flow curve characteristics typical of hydrogels. As a result, the viscosity values for the blank and lidocaine containing NLC gels were 4161.8 Pa·s and 4752.1 Pa·s, respectively, at a shear rate of 50 s^{-1} and at 25 °C. The API incorporated into the formulation resulted in a slight increase in viscosity, as observed from rheological curves.

On the other hand, the ointments showed high thixotropy compared to gels, which is typical in the case of water-free macrogol type ointments. The hysteresis area decreases in the presence of the active ingredient, indicating that the ointment undergoes more severe deformation without the active ingredient. The viscosity values for the blank and lidocaine containing ointments were 10841 Pa·s and 9962.5 Pa·s, respectively, at a shear rate of 50 s^{-1} and at 25 °C (Fig. 8).

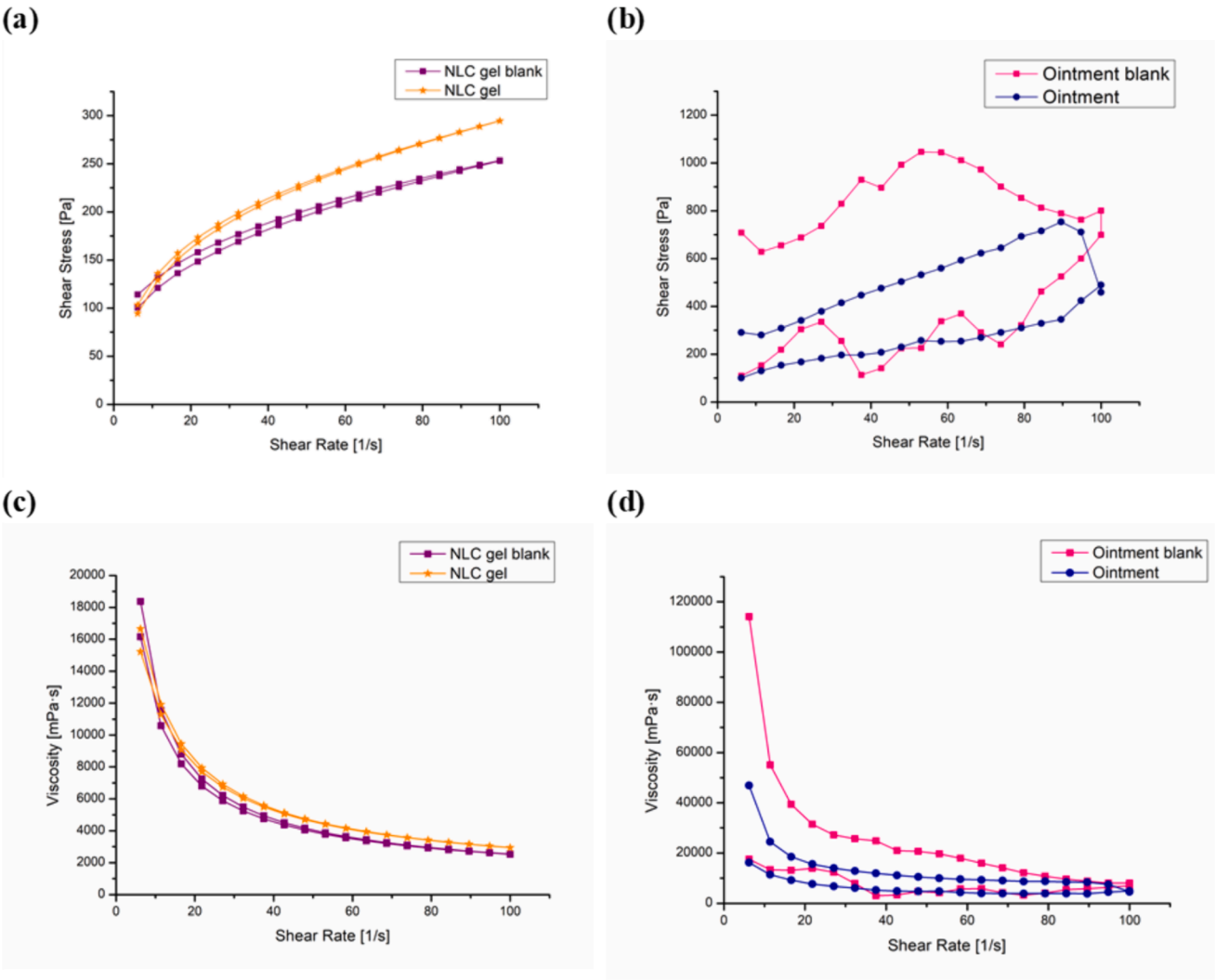

Fig. 8. Flow curves of the NLC gel and the blank sample (a), the ointment with and without lidocaine (b). The viscosity characteristics of both formulas (Pa·s) are presented in (c) and (d). The shear rate was initially increased from 0.01 to 100 s^{-1} (up curve) and then decreased from 100 to 0.01 s^{-1} (down curve) to assess possible hysteresis effects. Each data point represents the mean, n = 3.

The viscosity values of both systems were suitable for skin application, but more viscous formulations may predict slower drug diffusion in the matrix. This suggests that the rheological properties of the formulation can influence the drug release behaviour (Silva et al., 2012), (Marques et al., 2017).

3.3. Characterization of the 3D microneedle and penetration into the skin by fluorescence microscopy

Fluorescence confocal microscopy is a powerful imaging technique used to visualize structures in biological samples with high resolution. After the naked-eye observation of the images and the imprint of microneedles on the skin (Fig. 9a-b), the microscopic visualization of the 3D printed microneedle array was carried out to measure its actual dimensions after the printing process. The base of MNA was measured around 403 ± 10 μm (n = 12) with a distance of 908 ± 26(n = 14) μm between two bases from centre to centre (Fig. 8c) (Gittard et al., 2013). The MNA height and the microneedle height were 2 mm and 1 mm, respectively, which correlated well with the printing parameters design by CAD (Fig. 8d-e). A skin penetration depth up to 1 mm and an orifice of 281 ± 72 μm diameter n = 7 (Fig. 8 f-g) were observed. Based on the results, it was proven that the microneedles successfully pierced the skin barrier, therefore, an increased absorption of the active substance can be expected during the application of these tested MNAs. Two supplementary videos were prepared for the detailed exploration of microneedle dynamics in the skin. The first animation (S2) depicts the effects of the microneedle imprint on the skin surface, while the second animation (S3) shows a 3D animation of the skin's response to the microneedle imprint, providing insight into the depth changes within the skin.

3.4. Results of biopharmaceutical investigations

3.4.1. Results of IVRT

The *in vitro* release test of lidocaine from NLC gel and ointment formulations remained consistent over 6 h (Fig. 10). The release profiles were well-described by the Higuchi kinetic model. Higuchi's model describes release from an insoluble matrix as the square root of a time-dependent process based on Fickian diffusion (Paarakh et al., n.d.). Fig. 10 illustrates the Higuchi square root kinetics of both formulations, showing the cumulative amount of drug release versus the square root of time. The release constants, which represent the rate of the release, were calculated from the slopes of the appropriate plots, and the regression coefficients (R^2) were determined (Table 7). This kinetic model explains why the drug diffuses at a comparatively slower rate as the distance for diffusion increases, which is known as square root kinetics (Merchant et al., 2006). Furthermore, a significant difference was observed

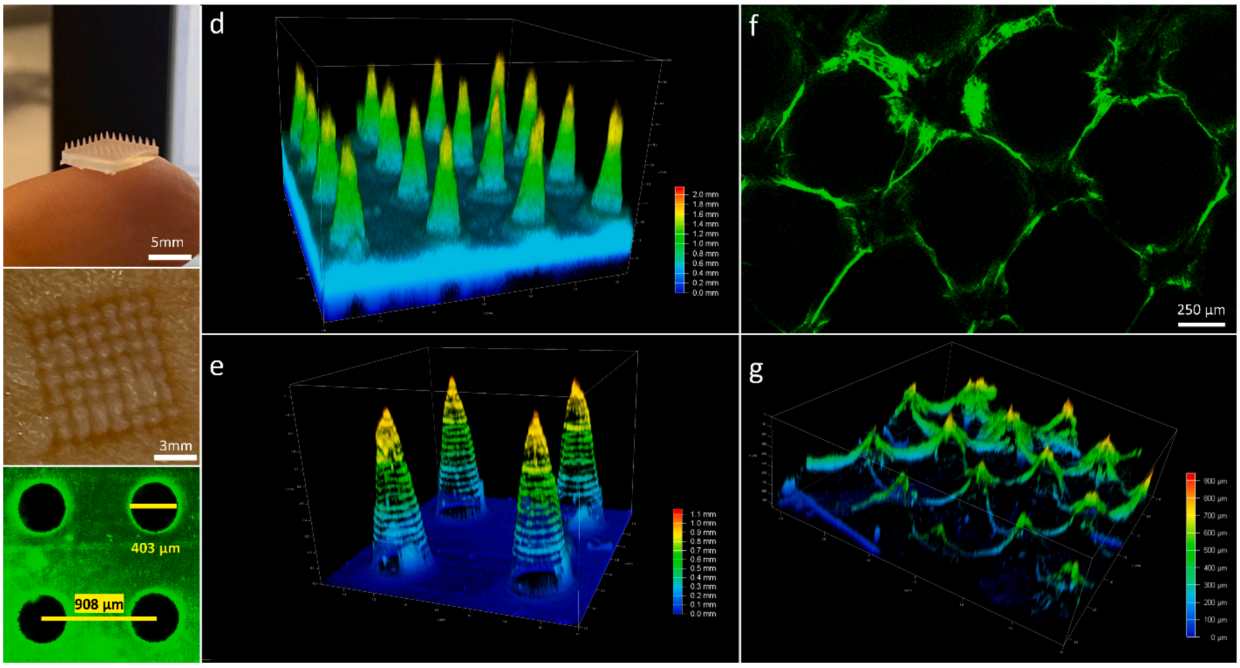

Fig. 9. Image of naked-eye observation of 3D printed microneedle array (a), visible imprint of microneedles on the skin (b), base of microneedle imaged with a confocal microscope labeled with curcumin solution (c), multiplane confocal optical sectioning and 3D reconstruction of microneedles labeled with curcumin solution using a 5x objective (d) and a 10x objective (e), single confocal optical section showing the surface of the skin after microneedle insertion and immediate removal of the MNA labeled with curcumin solution (f), multiplane confocal imaging and 3D reconstruction of the curcumin solution remaining in the skin immediately after the removal of the microneedle array (g). The colour intensity shows different heights from zero in blue to 2 mm in red.

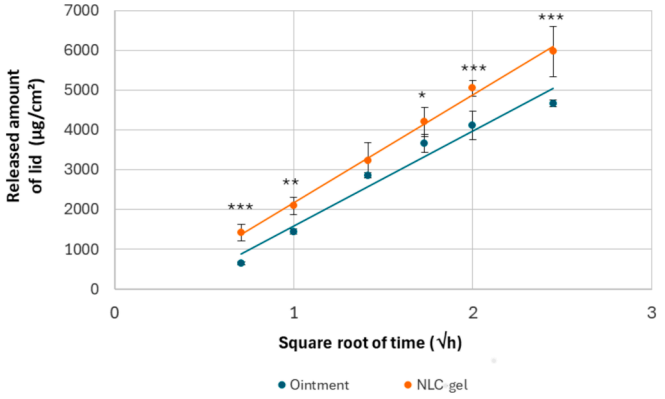

Fig. 10. In *vitro* release profile of the cumulative amount of lidocaine containing NLC gel and ointment formulation ($p \leq 0.05$ * $p \leq 0.01$ ** and $p \leq 0.001$ ***).

Table 7
Release parameters of lidocaine-loaded NLC gel and ointment.

Sample	Time (h)	Cumulative drug release (6 h)	R^2	Release constant
Ointment	6	4668.85	0.9656	309.53
NLC gel	6	5974.30	0.9962	349.3

between the released amount of lidocaine from the NLC gel (79 %) compared to the traditional ointment (48 %). This can be attributed to the distinct viscosities of the respective systems, which expalins why slower diffusion was detected from the ointment with higher viscosity.

3.4.2. Results of IVPT

While IVRT gives information about the performance of the formulation, IVPT shows the penetration of the active substance through the skin with the support of different carrier systems. In addition to the effect of the carrier system on permeation, 3D printed MNA was also tested as an active penetration enhancer method. The plots of the cumulative amounts of lidocaine permeated through heat-separated human epidermis as a function of time are shown in Fig. 11. The permeation parameters can be compared in Table 8. The difference between the two formulations is clearly visible. The skin permeation rate and the cumulative amount of lidocaine permeated from the NLC gel were 3.5 times higher than from the ointment, which was due to the nanosized carrier system. NLCs enhance skin penetration by interacting with skin layers and changing its barrier properties (Ghasemiyeh and Mohammadi-Samani, 2020). By pretreating the skin with microneedles, the skin permeation of lidocaine increased significantly. In the case of the ointment, about 2 times higher permeation rate was observed, while smaller improvement (about 1.2 times) was detected for the NLC gel. Based on the results, it can be concluded that comparing the two permeation enhancer methods investigated, the passive method (using an NLC carrier) improved permeation more effectively than the active method (using MN). Finally, when evaluating the effects of the two permeation enhancer methods (passive NLC and active MN) together, the results showed a synergistic effect on skin permeation, namely about 4.5 times higher permeation was measured compared to the result of the traditional ointment.

3.4.3. Results of Raman measurements

Raman scattering is a non-invasive and high spatial resolution spectral technique that provides fingerprint information on material structure (Binder et al., 2020; Kis et al., 2022). Several studies have reported that confocal Raman is an effective method for evaluating the penetration of active substances into the skin by mapping their distribution in the different skin layers (Kang and Zhang, 2022).

Raman mapping is a supporting measurement of the Franz diffusion cell method. In the case of IVPT, the quantitative amount of API permeated through the outermost epidermis layer of the skin can be measured, whereas in the case of Raman mapping, a qualitative

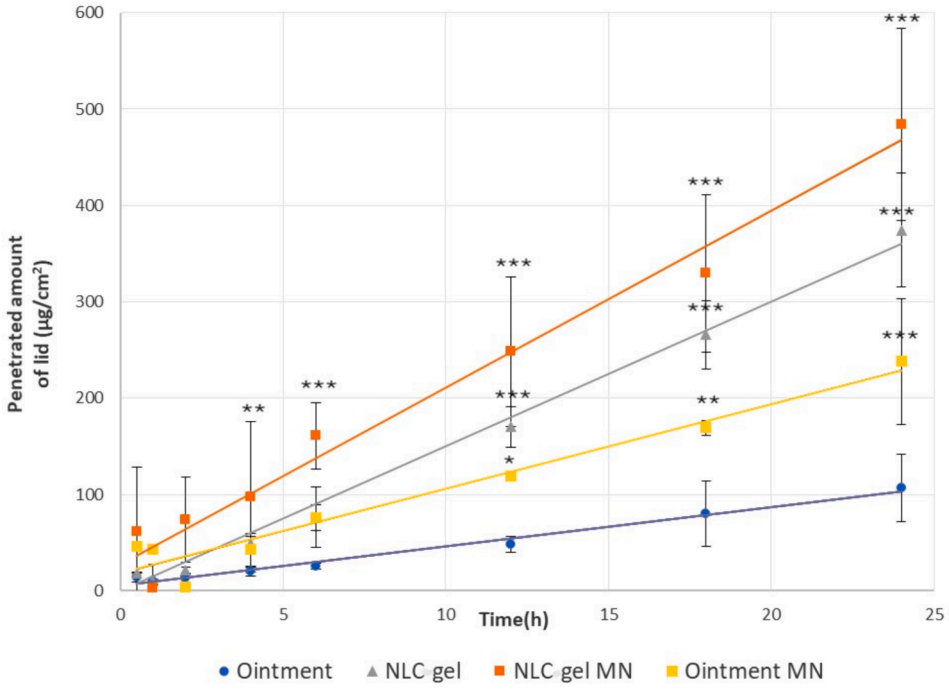

Fig. 11. In *vitro* permeation test of the cumulative plot of lidocaine-loaded NLC gel and ointment formulation with or without MNA pretreatment ($p \leq 0.05$ * $p \leq 0.01$ ** and $p \leq 0.001$ *** versus ointment).

Table 8
Permeation parameters of lidocaine-loaded NLC gel and ointment with or without microneedle pretreatment.

Sample	Time (h)	Cumulative drug permeation (24 h)	R^2	Permeation rate
Ointment	24	106.71	0.9869	4.0953
NLC gel	24	374.43	0.9966	15.01
Ointment MN	24	238.02	0.9516	8.7625
NLC gel MN	24	484.2	0.9774	18.364

measurement of API can be performed in the different layers of the skin (epidermis and dermis) (Zsikó et al., 2020).

Fig. 12 shows Raman correlation maps of skin treated with formulations with and without microneedle pretreatment. The blank formulations were the controls. The intense colour indicates the presence of lidocaine in the different skin layers.

In the case of the ointment, most of the API was detected in the middle part of the examined skin, which is located under the epidermis and in the upper part of the dermis. After pretreating the skin with microneedles, the API was also detected in the lower part of the dermis, which proves that the microneedle can promote the permeation of lidocaine into the deeper layers of the skin by destroying the barrier of the skin.

In the case of the NLC gel, the API was observed in the deeper layers of the skin, demonstrating the permeation-enhancing effect of the NLC system. Furthermore, concentrated API was detected in the epidermal layer, indicating the deposition of NLCs in this layer, probably due to their colloid size. After microneedle application, there was no further enhancement in permeation. This can be explained by the fact that the microneedle physically penetrates the skin barrier, helps the diffusion of NLC into the epidermal layer, but does not facilitate API permeation into deeper skin layers. It appears that NLCs penetrate the barrier, accumulate in the epidermal layer, act as a depot, and subsequently release the API into deeper skin layers.

4. Conclusion

One of the objectives of the study was to formulate and optimize NLCs, as a passive permeation enhancer system, with high drug loading capacity and adequate stability. Additionally, 3D printed solid microneedles were fabricated and characterized as active permeation enhancers for testing purposes. Lidocaine was chosen as the API, and lidocaine containing traditional ointment was used as a reference to demonstrate drug permeation without permeation enhancer methods. After formulating and characterizing two semisolid preparations (NLC gel and ointment), a comprehensive investigation from biopharmaceutical perspectives, including IVRT, IVPT, Raman mapping, was conducted. The study compared the passive (NLC system) and active (solid microneedles) permeation enhancement methods. It can be concluded that the passive permeation method was more effective than the active method for lidocaine permeation. Interestingly, when these methods were used together, a synergistic effect on skin permeation through the human epidermis (*in vitro*) was observed. However, when drug permeation into the deeper layer of the skin was evaluated by Raman mapping, the active method facilitated lidocaine permeation from the ointment, while there was no additional effect with the NLC system.

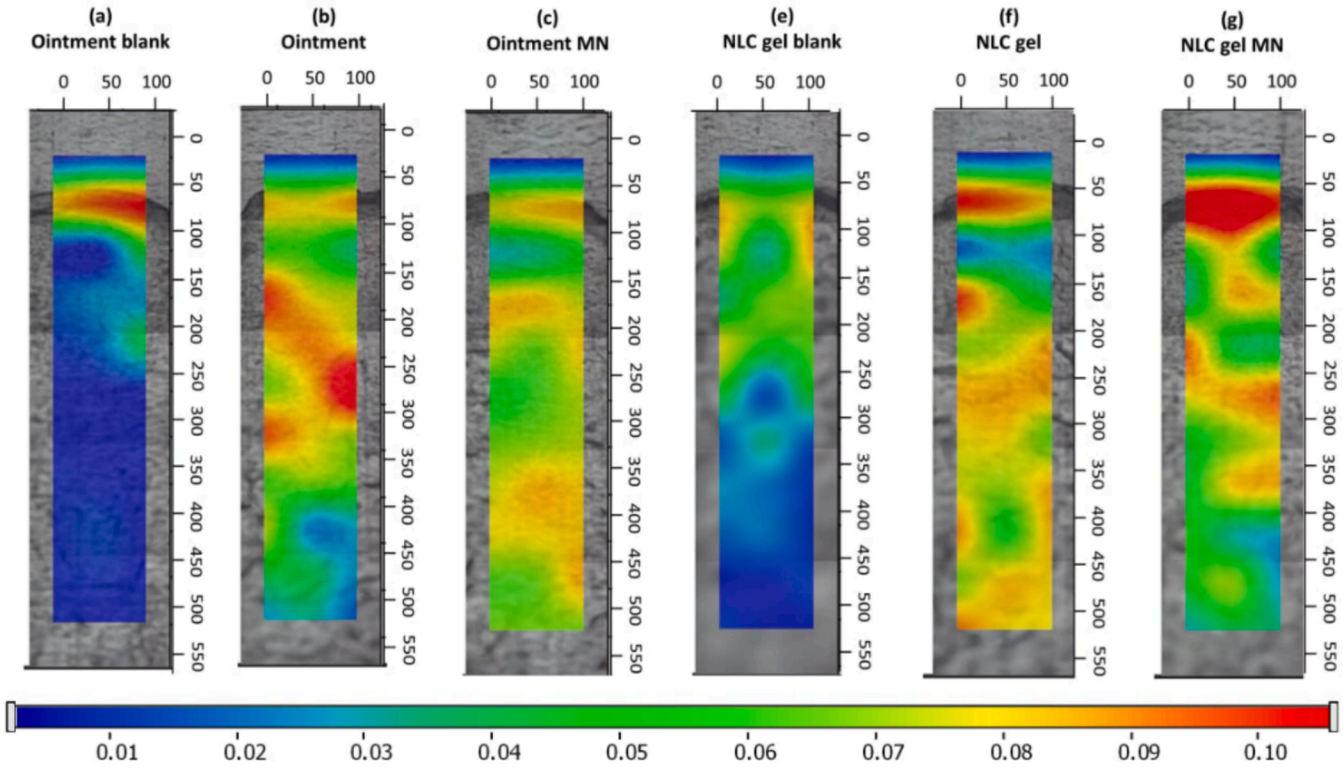

Fig. 12. Raman correlation maps of ointment blank (a), ointment containing lidocaine (b), ointment containing lidocaine with MNA pretreatment (c), compared with NLC gel blank (e), NLC gel containing lidocaine (f) and NLC gel with MNA pretreatment (g) in the excised human full skin samples.

CRediT authorship contribution statement

Feria Hasanpour: Writing – original draft, Visualization, Methodology, Investigation, Data curation. **Mária Budai-Szűcs:** Methodology, Investigation, Data curation. **Anita Kovács:** Supervision, Methodology, Data curation. **Rita Ambrus:** Methodology, Investigation. **Orsolya Jójárt-Laczkovich:** Methodology, Investigation, Data curation. **Martin Cseh:** Software, Methodology, Conceptualization. **Zsolt Geretovszky:** Methodology, Conceptualization. **Ferhan Ayaydin:** Visualization, Software, Methodology, Investigation, Conceptualization. **Szilvia Berkó:** Writing – review & editing, Supervision, Project administration, Funding acquisition, Conceptualization.

Declaration of competing interest

The authors declare the following financial interests/personal relationships which may be considered as potential competing interests: [Szilvia Berko reports article publishing charges was provided by University of Szeged (FundRef, Grant No. 6938). Ferhan Ayaydin reports financial support and equipment, drugs, or supplies were provided by EUs Horizon 2020 Research and Innovation Program (SGA No. 739593). Szilvia Berko reports financial support and equipment, drugs, or supplies were provided by TKP2021-EGA-32 has been implemented with the support provided by the Ministry of Culture and Innovation of Hungary from the National Research, Development and Innovation Fund. If there are other authors, they declare that they have no known competing financial interests or personal relationships that could have appeared to influence the work reported in this paper].

Data availability

Data will be made available on request.

Acknowledgements

The University of Szeged Open Access Fund (FundRef, Grant No. 6938) is also acknowledged for funding the open access publication.

Project no TKP2021-EGA-32 has been implemented with the support provided by the Ministry of Culture and Innovation of Hungary from the National Research, Development and Innovation Fund, financed under the TKP2021-EGA funding scheme.

F.A was supported by EU's Horizon 2020 Research and Innovation Program (SGA No. 739593).

Appendix A. Supplementary material

The following supporting information can be downloaded at S1: Results of the design of experiment and the adjustments. S2: Animation of the MNA imprint on the skin surface. S3: 3D animation of the skin's response to the microneedle imprint, providing insight into the depth changes within the skin.

Supplementary data to this article can be found online at https://doi.org/10.1016/j.ijpharm.2024.124377.

References

Ali, A., Ali, A., Rahman, M.A., Warsi, M.H., Yusuf, M., Alam, P., 2022. Development of nanogel loaded with lidocaine for wound-healing: illustration of improved drug deposition and skin safety analysis. Gels 8, 466. https://doi.org/10.3390/gels8080466.

Bahar, E., Yoon, H., 2021. Lidocaine: a local anesthetic, its adverse effects and management. Medicina 57, 782. https://doi.org/10.3390/medicina57080782.

Binder, L., Valenta, C., Lunter, D., 2020. Determination of skin penetration profiles by confocal Raman microspectroscopy: evaluation of interindividual variability and interlab comparability. J Raman Spectroscopy 51, 1037–1043. https://doi.org/10.1002/jrs.5871.

Brown, M.B., Martin, G.P., Jones, S.A., Akomeah, F.K., 2006. Dermal and transdermal drug delivery systems: current and future prospects. Drug Deliv. 13, 175–187. https://doi.org/10.1080/10717540500455975.

Chauhan, I., Yasir, M., Verma, M., Singh, A.P., 2020. Nanostructured lipid carriers: a groundbreaking approach for transdermal drug delivery. Adv Pharm Bull 10, 150–165. https://doi.org/10.34172/apb.2020.021.

Dabbagh, S.R., Sarabi, M.R., Rahbarghazi, R., Sokullu, E., Yetisen, A.K., Tasoglu, S., 2021. 3D-printed microneedles in biomedical applications. iScience 24, 102012. https://doi.org/10.1016/j.isci.2020.102012.

Economidou, S.N., Douroumis, D., 2021. 3D printing as a transformative tool for microneedle systems: recent advances, manufacturing considerations and market potential. Adv. Drug Deliv. Rev. 173, 60–69. https://doi.org/10.1016/j.addr.2021.03.007.

Economidou, S.N., Pere, C.P.P., Reid, A., Uddin, M.J., Windmill, J.F.C., Lamprou, D.A., Douroumis, D., 2019. 3D printed microneedle patches using stereolithography (SLA) for intradermal insulin delivery. Mater. Sci. Eng. C 102, 743–755. https://doi.org/10.1016/j.msec.2019.04.063.

Fudin, J., Wegrzyn, E.L., Greuber, E., Vought, K., Patel, K., Nalamachu, S., 2020. A randomized, crossover, pharmacokinetic and adhesion performance study of a lidocaine topical system 1.8% during physical activity and heat treatment in healthy subjects. JPR 13, 1359–1367. https://doi.org/10.2147/JPR.S238268.

Garutti, I., Rancan, L., Simón, C., Cusati, G., Sanchez-Pedrosa, G., Moraga, F., Olmedilla, L., Lopez-Gil, M.T., Vara, E., 2014. Intravenous lidocaine decreases tumor necrosis factor alpha expression both locally and systemically in pigs undergoing lung resection surgery. Anesth. Analg. 119, 815–828. https://doi.org/10.1213/ANE.0000000000000360.

Ghasemiyeh, P., Mohammadi-Samani, S., 2020. Potential of nanoparticles as permeation enhancers and targeted delivery options for skin: advantages and disadvantages. DDDT 14, 3271–3289. https://doi.org/10.2147/DDDT.S264648.

Gittard, S.D., Chen, B., Xu, H., Ovsianikov, A., Chichkov, B.N., Monteiro-Riviere, N.A., Narayan, R.J., 2013. The effects of geometry on skin penetration and failure of polymer microneedles. J. Adhes. Sci. Technol. 27, 227–243. https://doi.org/10.1080/01694243.2012.705101.

Gordh, T., Gordh, T.E., Lindqvist, K., Warner, D.S., 2010. Lidocaine: the origin of a modern local anesthetic. Anesthesiology 113, 1433–1437. https://doi.org/10.1097/ALN.0b013e3181fcef48.

https://www.iso.org/obp/ui/#iso:std:iso-astm:52900:ed-2:v1:en, n.d.

Janowska, A., Papa, G., Romanelli, M., Davini, G., Oranges, T., Stocco, C., Arnez, Z.M., Dini, V., 2022. 5% lidocaine hydrochloride cream for wound pain relief: a multicentre observational study. J. Invest. Surg. 35, 49–52. https://doi.org/10.1080/08941939.2020.1821134.

Kang, Y., Zhang, F., 2022. Image of the distribution profile of targets in skin by Raman spectroscopy-based multivariate analysis. Skin Res. Technol. 28, 402–409. https://doi.org/10.1111/srt.13114.

Khan, S., Sharma, A., Jain, V., 2023. An overview of nanostructured lipid carriers and its application in drug delivery through different routes. Adv Pharm Bull 13, 446–460. https://doi.org/10.34172/apb.2023.056.

Khurana, S., Jain, N.K., Bedi, P.M.S., 2013. Development and characterization of a novel controlled release drug delivery system based on nanostructured lipid carriers gel for meloxicam. Life Sci. 93, 763–772. https://doi.org/10.1016/j.lfs.2013.09.027.

Kis, N., Gunnarsson, M., Berkó, S., Sparr, E., 2022. The effects of glycols on molecular mobility, structure, and permeability in stratum corneum. J. Control. Release 343, 755–764. https://doi.org/10.1016/j.jconrel.2022.02.007.

L. Kiss, E., Berkó, S., Gácsi, A., Kovács, A., Katona, G., Soós, J., Csányi, E., Gróf, I., Harazin, A., Deli, M.A., Budai-Szűcs, M., 2019. Design and optimization of nanostructured lipid carrier containing dexamethasone for ophthalmic use. Pharm. 11, 679. Doi: 10.3390/pharmaceutics11120679.

Kovacevic, A., Savic, S., Vuleta, G., Müller, R.H., Keck, C.M., 2011. Polyhydroxy surfactants for the formulation of lipid nanoparticles (SLN and NLC): effects on size, physical stability and particle matrix structure. Int. J. Pharm. 406, 163–172. https://doi.org/10.1016/j.ijpharm.2010.12.036.

Lakkala, P., Munnangi, S.R., Bandari, S., Repka, M., 2023. Additive manufacturing technologies with emphasis on stereolithography 3D printing in pharmaceutical and medical applications: A review. Int. J. of Pharm.: X 5, 100159. https://doi.org/10.1016/j.ijpx.2023.100159.

Le, Z., Yu, J., Quek, Y.J., Bai, B., Li, X., Shou, Y., Myint, B., Xu, C., Tay, A., 2023. Design principles of microneedles for drug delivery and sampling applications. Mater. Today 63, 137–169. https://doi.org/10.1016/j.mattod.2022.10.025.

Lirk, P., Hollmann, M.W., Fleischer, M., Weber, N.C., Fiegl, H., 2014. Lidocaine and ropivacaine, but not bupivacaine, demethylate deoxyribonucleic acid in breast cancer cells in vitro. Br. J. Anaesth. 113 https://doi.org/10.1093/bja/aeu201 i32–i38.

Marques, A.C., Rocha, A.I., Leal, P., Estanqueiro, M., Lobo, J.M.S., 2017. Development and characterization of mucoadhesive buccal gels containing lipid nanoparticles of ibuprofen. Int. J. Pharm. 533, 455–462. https://doi.org/10.1016/j.ijpharm.2017.04.025.

Merchant, H.A., Shoaib, H.M., Tazeen, J., Yousuf, R.I., 2006. Once-daily tablet formulation and in vitro release evaluation of cefpodoxime using hydroxypropyl methylcellulose: a technical note. AAPS PharmSciTech 7. https://doi.org/10.1208/pt070378. E178–E183.

Milliken, R.L., Quinten, T., Andersen, S.K., Lamprou, D.A., 2024. Application of 3D printing in early phase development of pharmaceutical solid dosage forms. Int. J. Pharm. 653, 123902 https://doi.org/10.1016/j.ijpharm.2024.123902.

Müller, R.H., Müller, R.H., Mäder, K., Gohla, S., 2000. Solid lipid nanoparticles (SLN) for controlled drug delivery – a review of the state of the art. Eur. J. Pharm. Biopharm. 50, 161–177. https://doi.org/10.1016/S0939-6411(00)00087-4.

Paarakh, M.P., Jose, P.A., Setty, C., Peter, G.V., n.d. Release kinetics – concepts and applications.

Parhi, R., 2023. Recent advances in 3D printed microneedles and their skin delivery application in the treatment of various diseases. J. Drug Delivery Sci. Technol. 84, 104395 https://doi.org/10.1016/j.jddst.2023.104395.

Pathak, P., Nagarsenker, M., 2009. Formulation and evaluation of lidocaine lipid nanosystems for dermal delivery. AAPS PharmSciTech 10, 985. https://doi.org/10.1208/s12249-009-9287-1.

Preethi, G.B., Shivakumar, H.N., Kumar, M.R., 2022. 23 factorial design: an approach for formulation of solid lipid nanoparticles of etravirine for oral administration. IJPS 84. https://doi.org/10.36468/pharmaceutical-sciences.966.

Ramadon, D., Sutrisna, L.F.P., Harahap, Y., Putri, K.S.S., Ulayya, F., Hartrianti, P., Anjani, Q.K., Donnelly, R.F., 2023. Enhancing intradermal delivery of lidocaine by dissolving microneedles: comparison between hyaluronic acid and Poly(Vinyl Pyrrolidone) backbone polymers. Pharm. 15, 289. https://doi.org/10.3390/pharmaceutics15010289.

Reddy, M.R., Gubbiyappa, K.S., 2022. Formulation development, optimization and characterization of Pemigatinib-loaded supersaturable self-nanoemulsifying drug delivery systems. Future J. Pharmaceutical Sci. 8, 45. https://doi.org/10.1186/s43094-022-00434-4.

Shimojo, A.A.M., Fernandes, A.R.V., Ferreira, N.R.E., Sanchez-Lopez, E., Santana, M.H.A., Souto, E.B., 2019. Evaluation of the influence of process parameters on the properties of resveratrol-loaded NLC using 22 full factorial design. Antioxidants 8, 272. https://doi.org/10.3390/antiox8080272.

Silva, A.C., Amaral, M.H., González-Mira, E., Santos, D., Ferreira, D., 2012. Solid lipid nanoparticles (SLN) - based hydrogels as potential carriers for oral transmucosal delivery of risperidone: preparation and characterization studies. Colloids Surf. B Biointerfaces 93, 241–248. https://doi.org/10.1016/j.colsurfb.2012.01.014.

Sütő, B., Weber, S., Zimmer, A., Farkas, G., Kelemen, A., Budai-Szűcs, M., Berkó, S., Szabó-Révész, P., Csányi, E., 2015. Optimization and design of an ibuprofen-loaded nanostructured lipid carrier with a 23 full factorial design. Chem. Eng. Res. Des. 104, 488–496. https://doi.org/10.1016/j.cherd.2015.09.010.

Tetyczka, C., Hodzic, A., Kriechbaum, M., Juraić, K., Spirk, C., Hartl, S., Pritz, E., Leitinger, G., Roblegg, E., 2019. Comprehensive characterization of nanostructured lipid carriers using laboratory and synchrotron X-ray scattering and diffraction. Eur. J. Pharm. Biopharm. 139, 153–160. https://doi.org/10.1016/j.ejpb.2019.03.017.

Tfayli, A., Piot, O., Pitre, F., Manfait, M., 2007. Follow-up of drug permeation through excised human skin with confocal Raman microspectroscopy. Eur. Biophys. J. 36, 1049–1058. https://doi.org/10.1007/s00249-007-0191-x.

Treadwell, T., Walker, D., Nicholson, B., Taylor, M., Alur, H., 2019. Treatment of pain in wounds with a topical long acting lidocaine gel. CWCMR 6, 117–121. https://doi.org/10.2147/CWCMR.S224092.

Tulloch, A.P., 1970. The composition of beeswax and other waxes secreted by insects. Lipids 5, 247–258. https://doi.org/10.1007/BF02532476.

Uprit, S., Kumar Sahu, R., Roy, A., Pare, A., 2013. Preparation and characterization of minoxidil loaded nanostructured lipid carrier gel for effective treatment of alopecia. Saudi Pharmaceutical J. 21, 379–385. https://doi.org/10.1016/j.jsps.2012.11.005.

Witayaudom, P., Klinkesorn, U., 2017. Effect of surfactant concentration and solidification temperature on the characteristics and stability of nanostructured lipid carrier (NLC) prepared from rambutan (Nephelium lappaceum L.) kernel fat. J. Colloid Interface Sci. 505, 1082–1092. https://doi.org/10.1016/j.jcis.2017.07.008.

Xu, K., Wang, J., Yang, L., Wan, L., Wang, Y., 2019. Effect of lidocaine on the safety of postoperative skin reconstruction after malignant melanoma resection. Exp. Ther. Med. https://doi.org/10.3892/etm.2019.7519.

Yu, Y.-Q., Yang, X., Wu, X.-F., Fan, Y.-B., 2021. Enhancing permeation of drug molecules across the skin via delivery in nanocarriers: novel strategies for effective transdermal applications. Front. Bioeng. Biotechnol. 9, 646554 https://doi.org/10.3389/fbioe.2021.646554.

Zhang, F., Zhu, L., Li, Z., Wang, S., Shi, J., Tang, W., Li, N., Yang, J., 2021. The recent development of vat photopolymerization: a review. Addit. Manuf. 48, 102423 https://doi.org/10.1016/j.addma.2021.102423.

Zhao, X., Sun, Y., Li, Z., 2018. Topical anesthesia therapy using lidocaine-loaded nanostructured lipid carriers: tocopheryl polyethylene glycol 1000 succinate-modified transdermal delivery system. DDDT 12, 4231–4240. https://doi.org/10.2147/DDDT.S187177.

Zhou, D., Wang, L., Cui, Q., Iftikhar, R., Xia, Y., Xu, P., 2020. Repositioning lidocaine as an anticancer drug: the role beyond anesthesia. Front. Cell Dev. Biol. 8, 565. https://doi.org/10.3389/fcell.2020.00565.

Zsikó, S., Cutcher, K., Kovács, A., Budai-Szűcs, M., Gácsi, A., Baki, G., Csányi, E., Berkó, S., 2019. Nanostructured lipid carrier gel for the dermal application of lidocaine: comparison of skin penetration testing methods. Pharm. 11, 310. https://doi.org/10.3390/pharmaceutics11070310.

Zsikó, S., Csányi, E., Kovács, A., Budai-Szűcs, M., Gácsi, A., Berkó, S., 2020. Novel in vitro investigational methods for modeling skin permeation: skin PAMPA. Raman Mapping. Pharm. 12, 803. https://doi.org/10.3390/pharmaceutics12090803.